Unraveling the reinforcing mechanisms for cementitious composites with 3D printed multidirectional auxetic lattices using X-ray computed tomography

Meng, Zhaozheng; Xu, Yading; Xie, Jinbao; Zhou, Wen; Bol, Rowin J.M.; Liu, Qing feng; Šavija, Branko

Important note
To cite this publication, please use the final published version (if applicable).
Please check the document version above.

Unraveling the reinforcing mechanisms for cementitious composites with 3D printed multidirectional auxetic lattices using X-ray computed tomography

Zhaozheng Meng [a,*], Yading Xu [a], Jinbao Xie [a], Wen Zhou [a], Rowin J.M. Bol [a], Qing-feng Liu [b], Branko Šavija [a]

[a] *Microlab, Faculty of Civil Engineering and Geosciences, Delft University of Technology, Stevinweg 1, 2628 CN Delft, the Netherlands*
[b] *State Key Laboratory of Ocean Engineering, School of Ocean and Civil Engineering, Shanghai Jiao Tong University, Shanghai, China*

ARTICLE INFO

ABSTRACT

This study investigates the mechanical properties of cementitious composites with 3D-printed auxetic lattices, featuring negative Poisson's ratios (auxetic behavior) in multiple directions. These lattices were fabricated using vat photopolymerization 3D printing, and three base materials with varying stiffness and deformation capacities were analyzed to determine their impact on the composites' mechanical behavior. To unravel the reinforcing mechanisms of multidirectional auxetic lattices, which exhibit auxetic behavior in both planar and out-of-plane directions, X-ray computed tomography (X-ray CT) was utilized to analyze composite damage evolutions under different strain levels. The micro-CT characterization reveals that auxetic lattices more effectively constrain crack growth and dissipate energy by distributing stress evenly within the cement matrix. In contrast, due to lack of lateral confinement, the non-auxetic lattice reinforced composites primarily dissipate energy through extensive crack propagation and interfacial damage, leading to lower peak strength. When strain exceeding 5%, although the confinement from the auxetic behavior diminished with crack propagation, the lattice can still maintain the composite's structural integrity, resulting in 1.7 times higher densification energy than conventional cement-based materials. These findings provide valuable insights for designing auxetic lattice-reinforced cementitious composites with enhanced load-bearing capacity and improved dissipation capabilities.

1. Introduction

With the rapid advancement of additive manufacturing technologies, 3D printing has become a promising method for designing and manufacturing cementitious materials with engineered properties [1–3]. This innovation addresses the longstanding limitations of conventional cementitious composites, which have been fundamentally restricted by their inherent brittleness [4,5]. Under external load, microcracks will initiate from the cementitious matrix and propagate irreversibly into macrocracks, leading to premature cracking and even material failure under low strain conditions [6,7]. This has significantly constrained the suitability of cementitious materials for applications requiring high levels of ductility, energy absorption capacity, and post impact functionality [8,9]. Traditional solutions, such as steel reinforcements or fibers, have been employed to limit crack propagation and improve ductility [10,11]. However, the effectiveness of these methods is often limited by issues such as steel corrosion and the anisotropic nature of fiber distributions [12,13].

3D printed lattice structures have demonstrated their effectiveness in enhancing the ductility of cementitious materials [14–16]. By properly designing the architecture of 3D printed lattice structures, the desired mechanical properties of such cementitious composites can be engineered [17–19]. Among the various lattice architectures, auxetic lattices have received considerable attention for reinforcing cementitious composites due to their negative Poisson's ratio [20,21]. This counterintuitive behavior means that auxetic lattices will contract laterally under vertical compression, and expand laterally when stretched vertically, offering advantages such as large deformability, high energy absorption capacity, and excellent indentation resistance [22–24]. Typically, the auxetic behavior is achieved through specific structural designs that enable the unique deformation characteristics, including reentrant [25], chiral [26], and rotating units [27]. However, auxetic

---

* Corresponding author.
  E-mail address: z.meng@tudelft.nl (Z. Meng).

structures usually exhibit relatively low stiffness which prioritize flexibility and tailored deformation mechanisms over rigidity [28,29]. In contexts where certain load-bearing capacity is required, auxetic lattice structures can often be combined with stiffer materials such as cement-based materials to become composite materials, which enables the application in the field of civil engineering.

Recently, extensive studies have been conducted focusing on the mechanical properties of cementitious composites with auxetic structures [30,31]. Zhong et al. [32] filled a layered re-entrant manufactured by stacking aluminum sheets with the concrete matrix, and reported from the uniaxial compression tests that the auxetic structure can effectively enhance the peak stress and energy absorption capacity. Zhou et al. [33] conducted dynamic compression tests on the foam cement paste filled auxetic aluminum sandwich panels, and found that relative stiffness determined by the thickness of auxetic sandwich panels and matrix density had an obvious influence on the energy absorption performances. Zhao et al. [34] investigated the compressive behavior of cementitious composites with various lattice structures, each having an out-of-plane thickness of 45 mm. Their study showed that the cracking of the lattice reinforcement precipitates the failure of the overall composite structures, thereby preventing the composite material from reaching the densification stage. More recently, Xu et al. [35] fabricated two-dimensional polymeric auxetic frames (which show negative Poisson's ratio only in the loading plane) using the material extrusion (MEX) printing technique and subsequently filled these structures with cementitious matrix. Their findings indicated that reducing the volumetric ratio of the auxetic frame from 28 % to 14 % would result in a one-third reduction in terms of ductility. In addition, by using digital image correlation (DIC) analysis and finite element modelling (FEM), they also found that because of the lateral contraction on horizontal direction, the confinement from auxetic lattices causes limited crack propagation in the cementitious matrix [36].

Although planar auxetic structures can effectively enhance the ductility and even strength of cementitious composites, out-of-plane crushing has been reported in such cases [36,37], and planar auxetic structures usually require a larger thickness to avoid the out-of-plane buckling. Therefore, three-dimensional auxetic lattice structures have been designed and studied to harness their negative Poisson's ratio effect in multiple directions [38]. In most cases, three-dimensional auxetic lattice structures are designed by rotating two-dimensional auxetic slices on unit cell level [39,40]. Teng et al. [25] first designed a multidirectional re-entrant structure by composing two-dimensional slices, and they reported that the energy absorption capacity can be progressively improved by adding more two-dimensional slices. Furthermore, others could also be designed by connecting two planar auxetic structures by out-of-plane frames, and the Poisson's ratios can be adjusted by tunning the shape of the connecting frames [41]. As for its application in cementitious composites, Chen et al. [42] manufactured the three-dimensional auxetic structures (which show negative Poisson's ratios on both two directions under uniaxial loading conditions) by assembling printed beam components and embedding them into ultra-high performance concrete. They showed that with only 14 % volumetric reinforcement ratio, the auxetic lattice reinforced UHPC showed optimal energy absorption under high velocity impact loading. Besides, Hao et al. [43] tested cementitious composites with six different types of three-dimensional lattice structures printed by multi jet fusion technology. According to the acoustic emission signals in the elastic stage, they concluded that the 3D printed lattices can limit the damage initiation inside the cementitious matrix in the elastic stage during uniaxial compression.

According to the abovementioned literatures, remarkable contributions have been made to understand the mechanisms of two-dimensional auxetic lattice reinforced cementitious composites. In this case, the designed auxetic lattices only exhibited negative Poisson's ratios in the planar direction. However, few studies have focused on the mechanisms of multidirectional auxetic lattice reinforced cementitious composites,

where the auxetic lattices are designed to exhibit negative Poisson's ratio in both planar and out-of-plane directions. This is partly because manufacturing complex multidirectional lattice structures by traditional 3D printing techniques such as material extrusion remain challenging. More importantly, when utilizing multidirectional structures, it is difficult to capture the damage situations insides the composite materials, as the external surface layer always crumbles first because of lack of confinement, making surface observation techniques less efficient. Additionally, multidirectional lattice structures possess different mechanical features with traditional planar ones, owing to the nature of different manufacturing technologies. For traditional planar structure made by material extrusion, the side surface is commonly enclosed by continuously stacked filaments. In this case, superior in-plane stiffness is present, together with a weakened out-of-plane buckling resistance. In contrast, multidirectional lattice structures offer more balanced confinement in both in-plane and out-of-plane directions. Therefore, further research is necessary to elucidate the mechanical properties and reveal the underlying mechanisms of cementitious composites reinforced with multidirectional auxetic lattice structures.

In this study, uniaxial compression tests were conducted on cementitious composites reinforced with multidirectional auxetic and non-auxetic lattice structures. The lattices were printed by the vat photopolymerization (VPP) method, allowing for the high-resolution fabrication of complex multidirectional lattice structures. In addition, three kinds of printing materials with different stiffnesses, elongation capacity, and hardness were utilized to probe the influence of material properties of lattices structures on the overall responses of the composites. The energy absorption capacity of cementitious composites with auxetic and non-auxetic lattices were also quantified. Most importantly, to unravel the internal damage situations of the cementitious composites, ex-situ X-ray computed tomography (X-ray CT) tests were conducted under three strain levels to analyze the crack distributions, aiming to provide more insights into the functioning mechanisms of multidirectional auxetic lattice structures.

2. Materials and Experiments

2.1. Design and manufacturing of multidirectional auxetic structures

The design process of the multidirectional auxetic structure is shown in Fig. 1. In planar configurations, the "rotating square" structure was first designed by substituting solid squares with struts, as shown in Fig. 1 (a) and Fig. 1(b). This modification enables the structure to remain achieving its auxetic mechanisms through joint buckling, while allowing the infiltration of cementitious matrix. To transition from a two-dimensional structure into a three-dimensional one, two parallel 2D structures were positioned at a certain distance to form the horizontal frame, shown by Fig. 1(c). The horizontal frame was then vertically interconnected by struts, as colored in green in Fig. 1(d). However, despite achieving a three-dimensional configuration, the auxetic behavior remains in-plane (i.e., contraction occurs only in one direction under uniaxial compression). To induce auxetic behavior in all directions, the struts were further rotated around their central axis at a certain angle (45° in this study), resulting in a unit cell with multidirectional auxetic properties, as shown in Fig. 1(e). The final 3D rotating square structure, shown in Fig. 1(f), comprises a 2 × 2 × 2 array of unit cells. The diameter of the struts is set as 1.5 mm, and the overall structure dimension is 18 × 18 × 18 mm^3 with a total volume of 1480 mm^3.

For comparison, non-auxetic octet and cubic shaped structures have also been included. Table 1 presents the dimensions and geometrical representations of the 3D lattice structures. It should be noted that the strut thicknesses for the octet and grid structures were designed as 1.2 mm and 1.6 mm respectively, to match the total volume of the auxetic rotating square structure, thereby ensuring a fair comparison. In addition, mini dog-bone specimens were designed for testing the material
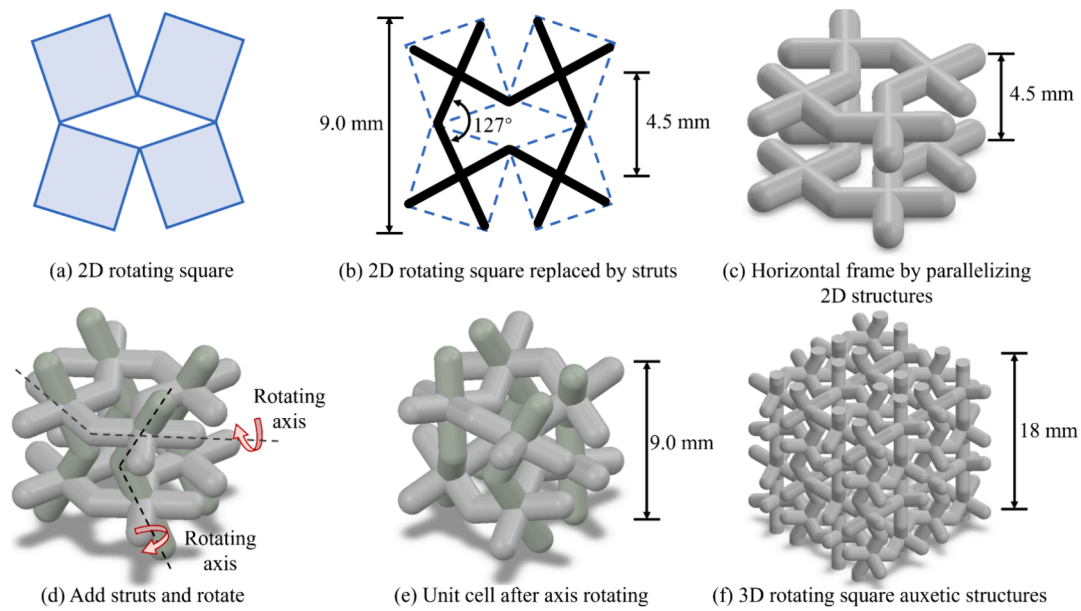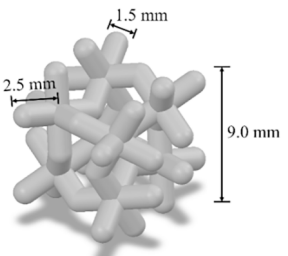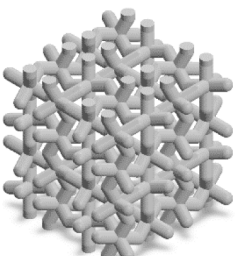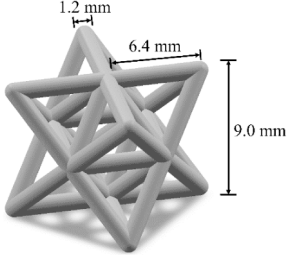
(a) 2D rotating square

(b) 2D rotating square replaced by struts

(c) Horizontal frame by parallelizing 2D structures

(d) Add struts and rotate

(e) Unit cell after axis rotating
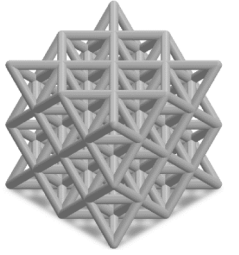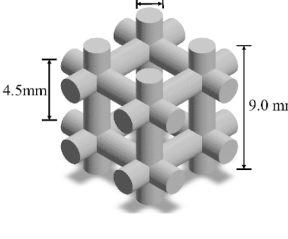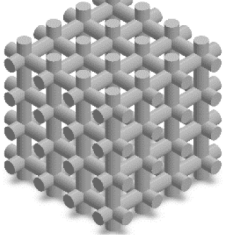
(f) 3D rotating square auxetic structures

Fig. 1. The schematic overview of the designing process for multidirectional rotating square auxetic structures.

Table 1
Geometrical representations of designed structures.

Type	Unit cell	3D structures	Volume
Rotating square (RS)			1480 mm³
Octet (OCT)			1420 mm³
Cubic (CB)			1440 mm³

properties, and the dimensions and printing direction are illustrated in Fig. 2.

The designed lattice structures were fabricated using VPP printing techniques, which can print complex 3D structures with higher resolution and versatile materials easier than the conventional material

extrusion techniques. The basic principles of VPP lie in the photopolymer resins solidifying under the exposure of ultraviolet (UV) light. The parts are printed layer by layer, with each layer exposed to a UV light pattern as specified by the slicer software which divides the 3D model into horizontal layers. In this study, the ELEGOO Mars 3 resin 3D
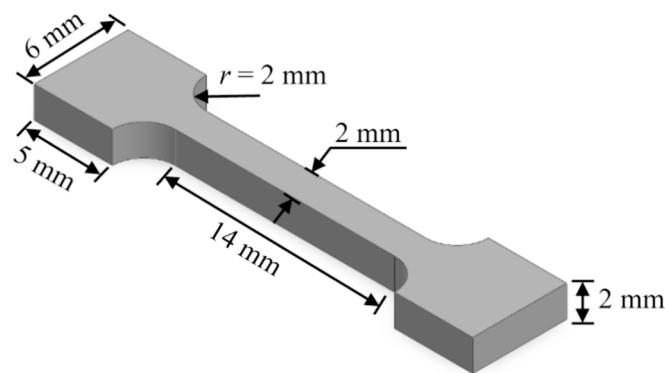
Fig. 2. Dimensions of mini dog-bone specimens.

Table 3
Mixing proportions of cementitious matrix (g/L).

Water-to-binder ratio	CEM I 42.5 N	Fly ash	Fine aggregates (0.125–0.250 mm)	Water	Superplasticizer (Glenium 51)
0.4	615	728	616	538	2.6

printer was used for manufacturing the lattice structures. Three different photopolymer resins were employed as base materials: Elegoo Plant-based Resin (general-purpose resin), Loctite 3D IND405 High Elongation Resin (high elongation resin), and Formlabs Rigid 10 K Resin (high rigidity resin), abbreviated as G, E, and R respectively. The printing parameters are summarized in Table 2. The exposure time denotes the duration each layer is exposed to UV light, which is usually longer for bottom layers to ensure a better bonding between the printed parts and building plate. The light-off delay is a time interval between the completion of one layer and the start of the next layer's exposure to UV light, which is usually included for highly viscous resins to ensure a correct position of the next layer. After printing, the lattices were exposed to 405 nm UV light for five minutes for post-processing.

2.2. Preparation of cementitious composites

The size of the cementitious composite sample was 20 mm × 20 mm × 20 mm in cubic shape. The mixture proportions of the cementitious matrix are listed in Table 3, where the fine aggregate mortar was used to ensure complete infiltration of the lattice structures. Cement, fly ash, and fine aggregates were first mixed using the Hobart N50 planetary mixer for 4 min. Subsequently, water and superplasticizer were added, followed by an additional 4-minute mixing period. The mortar was then cast into silicon molds where the 3D printed lattice structures were glued to prevent them from moving during subsequent vibration. The specimens were subsequently vibrated for 30 s to ensure a uniform distribution of the matrix. After 2 days, the specimens were demolded and cured in an environment with a temperature of 20 ± 2 °C and a relative humidity of 96 ± 2 % until reaching 28 days of age. The preparation process of the cementitious composites is shown in Fig. 3.

2.3. Mechanical tests

The UNITRONIC S205N universal loading stage was used to conduct uniaxial compression tests on both the 3D printed lattice structures and the cementitious composites. As shown in Fig. 4(a), specimens were placed between two steel plates, and the contact surfaces were greased with lubricating oil to reduce the boundary friction. The measurements of two linear variable differential transformers (LVDTs) were averaged to eliminate the errors caused by loading frame rotation. The loading rate was kept as 0.01 mm/s controlled by the averaged displacement value from two LVDTs. In total, 9 groups of 3D printed lattice

reinforcements (three kinds of architectures printed by three printing materials), and 9 groups of corresponding cementitious composites were prepared. For each group of lattice reinforcement and composites, three duplicate specimens were prepared to ensure the repeatability, and the results were averaged. During the compression test of 3D printed lattice structures, photographs were systematically captured at a five-second interval to record the deformation states and failure modes of the structures. As for the material property tests, a small tensile testing machine (TSM) with a load cell range of 500 N was used. As displayed in Fig. 4(b), the dog-bone shaped specimens were clamped on both sides, and a loading rate of 0.01 mm/s was also used.

2.4. CT scanning

For cementitious composites reinforced by 3D printed lattice structures, CT scans were conducted to observe the internal damage under different loading conditions. The micro-CT scanner (Phoenix X-ray Nanotom μ-CT scanner) was used, operating at a tube voltage of 120 kV and current of 125 mA. During scanning, the samples were rotated 360°, resulting in the acquisition of 2880 projections stored as 16-bit image files with grey-scale values from 0 to 65536. The sensor resolution was chosen as 1920 × 1896 pixels with a pixel size of 15 μm. To compare the crack distributions under different loading levels, 3 ex-situ CT scans were conducted for each specimen: loading the specimen until 0.5 mm and unloading to the first scan; re-loading to 1.0 mm and unloading again to conduct the second scan; re-loading to 1.5 mm and unloading for the third scan. The results were reconstructed using StudioMax software and visualized with Dragonfly 3D to examine the internal crack information within the matrix.

3. Results and discussions

3.1. Material properties of the 3D-printed resin

The tensile engineering stress–strain curves of the specimens fabricated using three different resins are presented in Fig. 5. The mechanical properties have also been summarized in Table 4. It can be noticed that only high elongation resin showed ductile behavior after the initial peak stress, achieving a fracture strain of up to 62.5 % without any observed softening prior to cracking. The reason for such a ductile behavior is that the high-elongation resin could generate less rigid crosslinks during the polymerization process. With a lower crosslink density, longer polymer chains can be formed, which can reduce the risk of brittle failure at crosslinks and improve the ductility [44]. The high rigidity resin showed superior performance in terms of initial stiffness and peak stress, which can reach 7.0 GPa and 82.8 MPa, respectively. In contrast, the general-purpose resin exhibited an initial stiffness comparable to that of the high elongation resin at 1.4 GPa, but its strength was 28.2 MPa with no plastic deformation stage observed before fracturing at a strain of 2.1 %. It should be noted that, as a nature of 3D printing techniques, mechanical

Table 2
Printing parameters for different photopolymer resins.

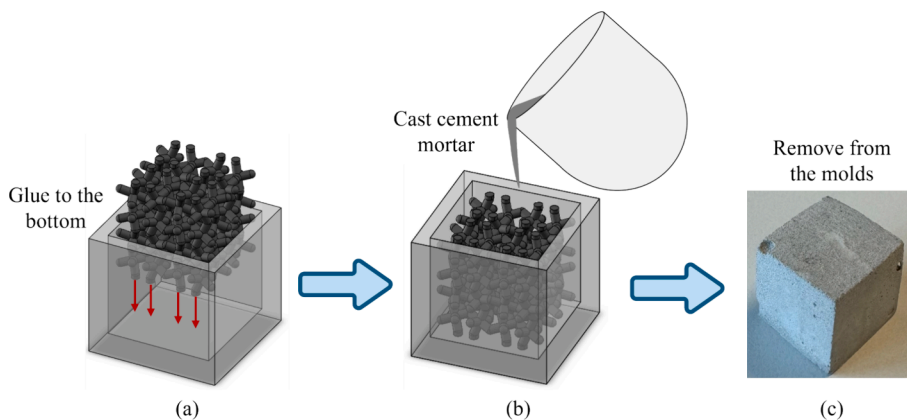| Resin types	Layer thickness (μm)	Normal layer exposure time (s)	Bottom layer exposure time (s)	Bottom layer number	Light-off delay (s)
General-purpose	50	2.5	35	8	–
High elongation	50	12	35	8	6.5 s
High rigidity	50	16	80	8	6.5 s

Fig. 3. Specimen preparation procedure: (a) 3D reinforcement glued in silicon mold, (b) casting fresh mortar, and (c) specimens after demolding.
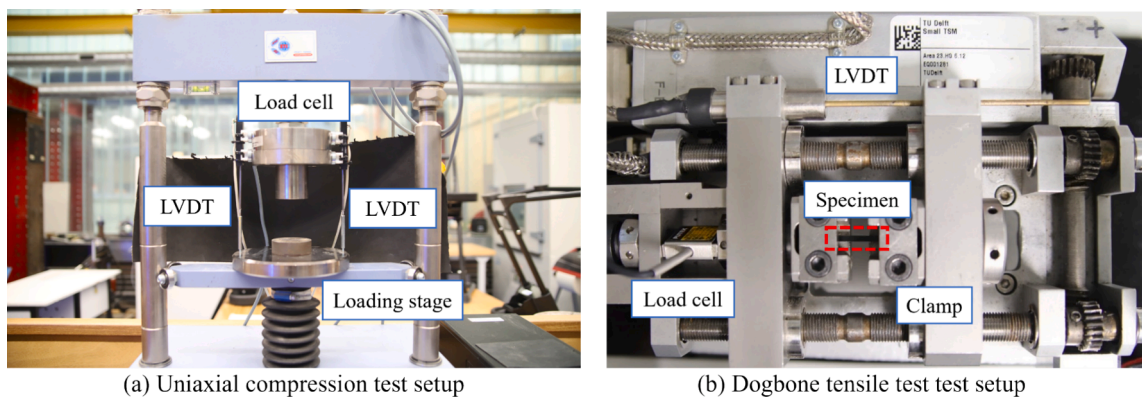

(a) Uniaxial compression test setup   (b) Dogbone tensile test test setup

Fig. 4. Experiment set-up for (a) uniaxial compression test and (b) dog bone tensile test.
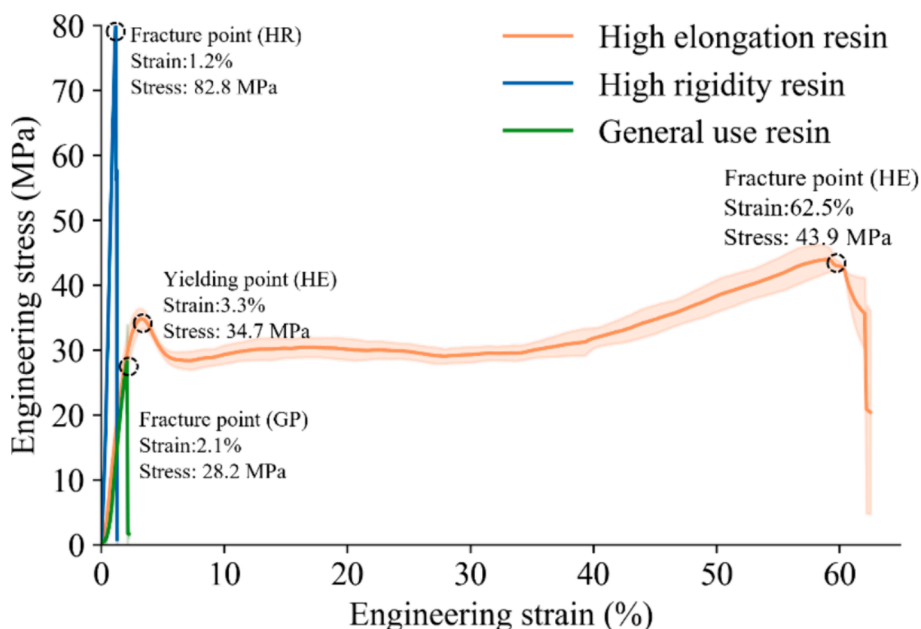

Fig. 5. Engineering stress–strain curves for dog bone specimens 3D printed by different resins (the solid lines denote the average values and shaded areas indicate the deviations).

properties of 3D printed specimens are influenced by the printing direction [45,46], while the present study only reported the mechanical properties on one direction (i.e., parallel with the printing direction) to showcase different material features.

In addition, compared to traditional MEX printing techniques where significant anisotropy can be induced due to the weak bonding between

Table 4
Mechanical properties of three used resins.

Resin types	Elastic modulus	Tensile stress at yield	Elongation at yield	Tensile stress at fracture	Elongation at fracture
General-purpose	1.4 GPa	–	–	28.2 MPa	2.1 %
High rigidity	7.0 GPa	–	–	82.8 MPa	1.2 %
High elongation	1.7 GPa	34.7 MPa	3.3 %	43.9 MPa	62.5 %

two adjacent layers, the layer adhesion is stronger in VPP printed samples since the layers are formed by fully curing liquid resin with a UV light. Fig. 6 displays the CT scanning results of the dog bone specimens printed by MEX and VPP techniques, where a resolution of 6 μm was achieved under a tube voltage of 60 kV and current of 250 mA. The printing parameters for the MEX method can be found in literature [35], and the printing direction can be found in Appendix A. The printing parameters for the VPP printed specimen are identical with those for high elongation resin as mentioned in Table 2. As shown in Fig. 6(c), the CT determined defect density for the sample printed by the MEX method was 1.46 %, and defects showed distinct patterned distributions due to the layer-by-layer deposition method. The defects were almost continuous from the bottom end to the top end, and the defects were also located between two adjacent layers, suggesting that severe anisotropy could be observed in the mechanical performances of MEX printed samples. On the contrary, the defect density for the sample printed by the VPP method was only 0.01 %, and it can be found from Fig. 6(d) that the defects insides the VPP printed sample were generally air bubbles inside the hardened resin, where the defects have been enlarged two times to ensure a clear visibility. These pores were randomly distributed inside the sample, and did not show any obvious distribution patterns which are aligned with the printed layers, which suggests that the anisotropy may be not that significant compared to MEX printed samples. Moreover, the defect volume distributions were also compared in Fig. 7. It can be found that the defect volumes for MEX printed samples were generally distributed between 0 and 0.001 mm^3, and there were some larger imperfections with a volume beyond 0.001 mm^3 which could be the internally connected voids between two printing layers. On the contrary, the majority of defects in VPP printed samples were in the smallest defect size range that can be distinguished by the CT scanning, which suggests that the imperfection distribution was more uniform.
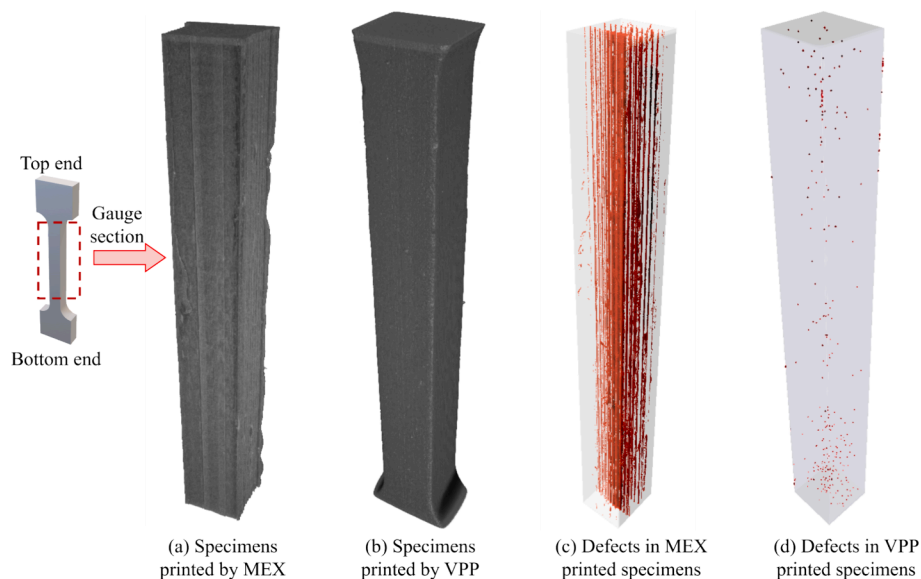

Fig. 7. Defect volume distributions obtained by CT images for MEX and VPP printed specimens.

3.2. Mechanical performances of 3D-printed lattice structures

The stress–strain curves of auxetic and non-auxetic lattices printed by different resins are displayed in Fig. 8. Lattices printed by the high-rigidity resin exhibited the highest strength and initial stiffness but the lowest ductility, and also went through the most severe brittle failure. As displayed in Fig. 9(a)~(c), the failure pattern for these structures was brittle, where splash of the broken struts was observed from the camera. Consequently, the stress–strain curves of high-rigidity lattices exhibited a sharp decline after reaching the peak stress, which was due to the brittleness of the printing base material.

For lattices printed using general-purpose resin, the failure process was generally less abrupt. In the rotating square and octet structures shown in Fig. 8 (a) and Fig. 8 (b), stresses started to decline after the

Fig. 6. CT scanning results of (a) dog bone specimen printed by MEX, (b) dog bone specimen printed by VPP, (c) defects insides MEX printed specimen, and (d) defects insides VPP printed specimen, where only the gauge regions (parallel section) were displayed here as the region of interest.
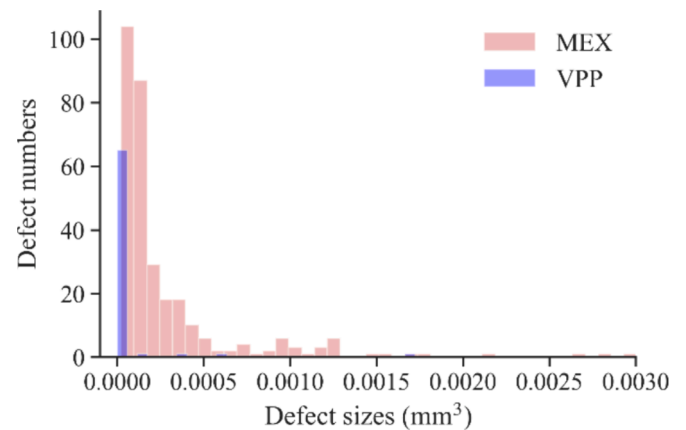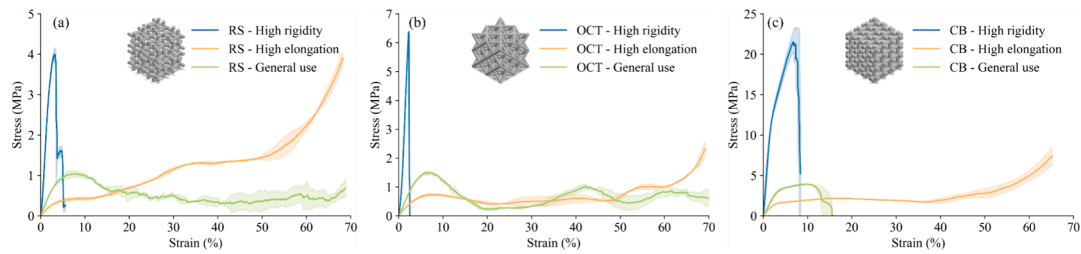
Fig. 8. Stress–strain curves of (a) rotating square, (b) octet, and (c) cubic lattice structures 3D-printed by different resins (the solid line denotes the average values, and shaded area indicates the deviation).
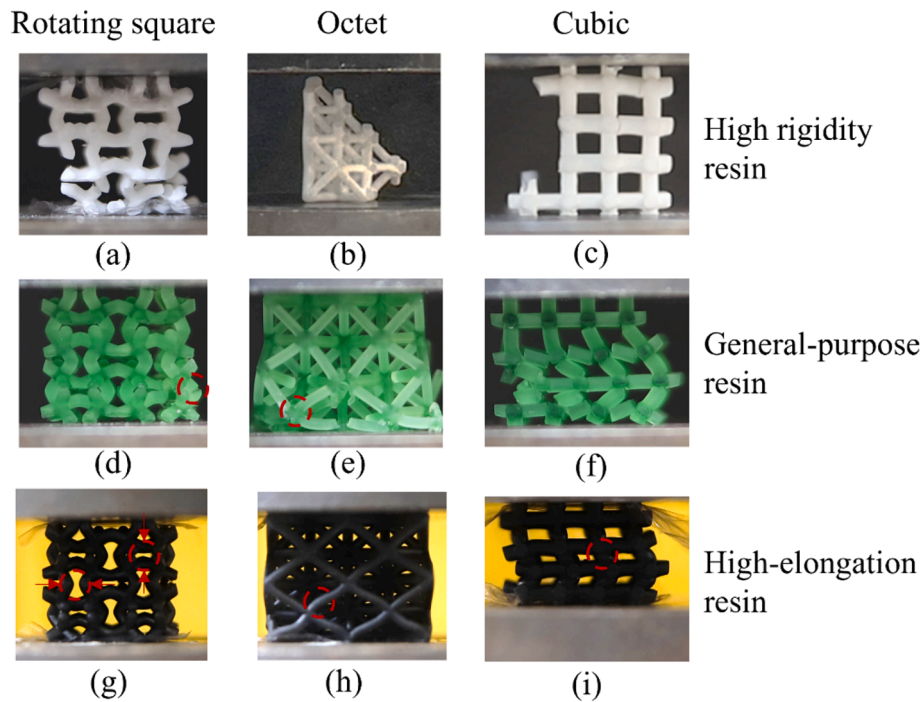

Fig. 9. Failure modes of 3D printed structures with different architectures and printing materials: (a)~(c) rotating square, octet, and cubic lattice printed by high rigidity resin; (d)~(f) rotating square, octet, and cubic lattice printed by general-purpose resin; (g)~(i) rotating square, octet, and cubic lattice printed by high-elongation resin.

initial crack appeared. However, since the peak stress was lower (below 2 MPa) compared to those printed with the high-rigidity resin (above 4 MPa), the energy released upon fracture was insufficient to completely break the entire cross section. Therefore, these lattices did not show abrupt failure. This is supported by Fig. 9(d) and Fig. 9(e), where some cracks did not fully penetrate the entire cross-section (indicated by the red dashed circle), allowing the damaged lattice struts to maintain some contact with other parts of the structure, which led to a gradual decline in the post-peak branch. However, as shown in Fig. 8(c), the cubic lattice printed with general-purpose resin displayed brittle failure at a strain level of about 12 %. This occurred because the cubic structure is more aligned with the loading direction, resulting in a higher energy release upon fracture, which fully broke the cross-section of the struts, as seen in Fig. 9(f). Consequently, the lattice lost its integrity, ultimately leading to a drop in stress level to zero.

On the contrary, the lattices printed by high elongation resin only showed local buckling at the joints instead of cracking. For the rotating square auxetic lattice, the stress–strain curves continued to increase rather than fluctuate as observed in the octet and cubic lattices. This behavior can be attributed to the joints buckling inward (as indicated by the red dashed circle in Fig. 9(g)) and eventually contacting with each other due to the auxetic nature of the structure. As a result, the buckling of the struts did not lead to a reduction in load-bearing capacity.

However, in the octet and cubic lattices, the buckling of the struts could not form new contacts as shown in Fig. 9(h) and Fig. 9(i), so the stress levels continued fluctuating until the full densification was reached. Nevertheless, when utilizing the high elongation resin as the base material, no cracking occurred in all three kinds of lattices until the end of the test, suggesting that the fracture behavior of 3D-printed lattices were more related to the material properties.

The Poisson's ratios printed with the high elongation resin were calculated and shown in Fig. 10, where the Poisson's ratio here is defined as the ratio between horizontal displacement and vertical displacement of the lattice specimens (i.e., the global Poisson's ratios for the lattice structure). It is noteworthy that, due to the premature cracking and loss of structural integrity in lattices printed with the high rigidity resin and the general-purpose resin, only rotating square lattices printed with the high elongation resin showed negative Poisson's ratios. This indicates that, despite the architectural design intended to achieve a negative Poisson's ratio, material brittleness can inhibit the auxetic behavior. As shown in Fig. 10, the Poisson's ratios of auxetic lattice (RS) were initially negative, and then turned into positive stage because of the densification of the structure and the contact of adjacent joints displayed in Fig. 9(g). In addition, the Poisson's ratios of auxetic lattice structures in the other direction are also shown in Fig. 11. It can be found that the designed rotating square lattice structures showed auxetic
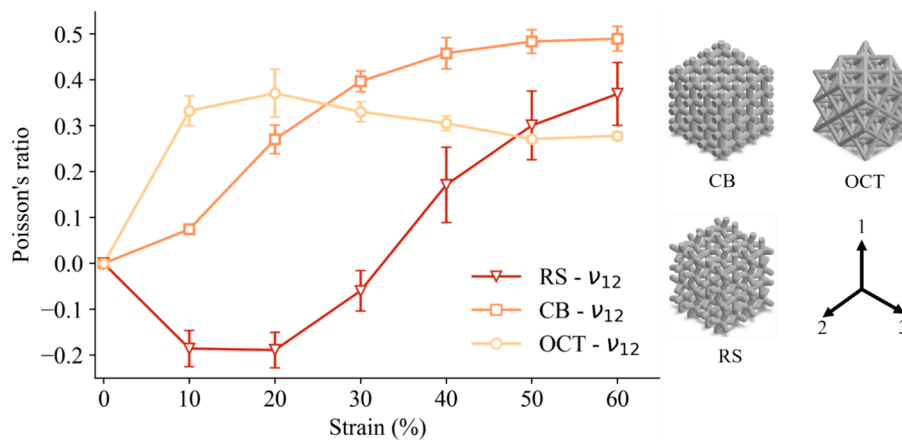
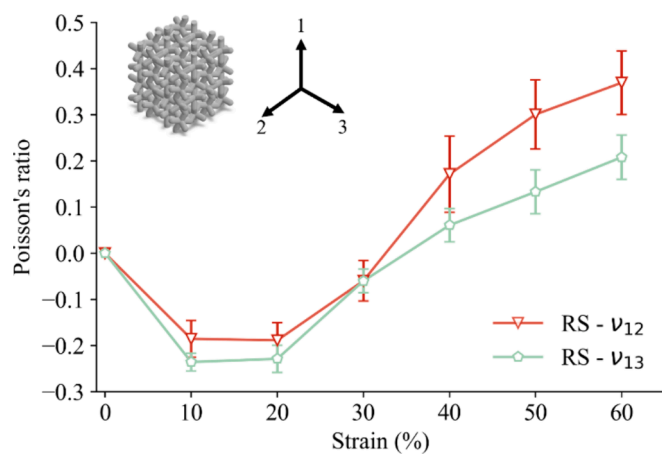**Fig. 10.** Global Poisson's ratios for lattice structures printed by resin with high elongation capacity.

Fig. 11. Poisson's ratios of rotating square (auxetic lattice structures) on two directions.

Fig. 12. Stress–strain curves for rotating square auxetic lattices tested along three principle directions.

behaviors in both directions, suggesting that the confinement on the cementitious matrix could exist in both directions. Conversely, The Poisson's ratios of cubic shaped lattices were initially lower compared to these of octet structures but became increasingly more positive after reaching 10 % strain, due to the local buckling near the joints, as shown in Fig. 9(i).

To further explore the anisotropy of the designed auxetic lattice structures, the high-elongation resin printed auxetic lattices were tested along three principal directions, and the results have been shown in Fig. 12. No obvious anisotropy can be captured from the testing results. This is mainly because the auxetic lattice was composed by a unit cell array of 2 × 2 × 2, so the arrangement of the unit cells along each direction was the same with each other. Besides, this can be also attributed to the less anisotropy of VPP 3D printing method where no patterned defects were observed between two adjacent printing layers. Therefore, also considering the symmetrical nature of octet and cubic lattices, the subsequent results for cementitious composites were compared and discussed based on the compression test in direction one.

3.3. Mechanical performance of cementitious composites

3.3.1. Stress–strain curves

The compressive stress–strain curves of cement mortar (reference group) and cementitious composites embedded with 3D-printed auxetic structures (rotating square) are presented in Fig. 13(a) and (b), respectively. It can be seen from the figure that the inclusion of 3D printed lattice structures in cementitious materials leads to a lower initial
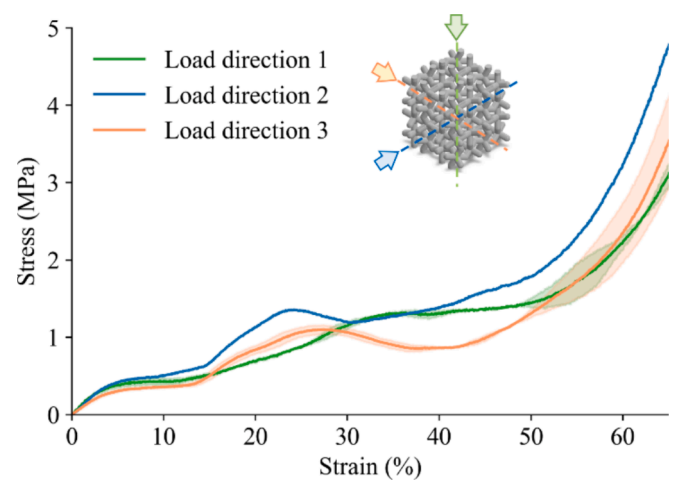
stiffness compared to that of the reference group. This can be attributed to the introduction of a material phase that is less stiff than the cementitious mortar. It can also be observed that the peak strain at maximum stress increased from 2.7 % in the reference group to approximately 4.5 % on average for cementitious composites containing auxetic lattice structures. In addition, the composites reinforced by the high rigidity rotating square-shaped lattice structures exhibited comparable strength to the reference group, while auxetic lattice structures printed with high elongation resin led to an overall reduction in composites' strength.

However, unlike the reference group where stresses dropped sharply after the peak, the cementitious composites with auxetic lattices printed using high elongation resin exhibited improved post-peak ductility. After the peak stress of 14 MPa, the stress stabilized at approximately 10 MPa, forming a plateau before entering the densification stage, where the stress increased exponentially. However, in terms of lattices printed by high rigidity resin and general-purpose resin, their role in improving the post-peak ductility is less pronounced, where the stresses of composites dropped to nearly zero. This behavior can be attributed to the brittleness of the lattice structures printed with these resins. After the failure of lattices within the cementitious matrix, the fractured parts acted as flaws of the matrix, diminishing the load bearing capacity of the composites. On the contrary, lattices printed with high elongation resin maintained their structural integrity until the densification stage, thereby preserving the integrity of the composites and enabling the improved post-peak ductility. This highlights the importance of using
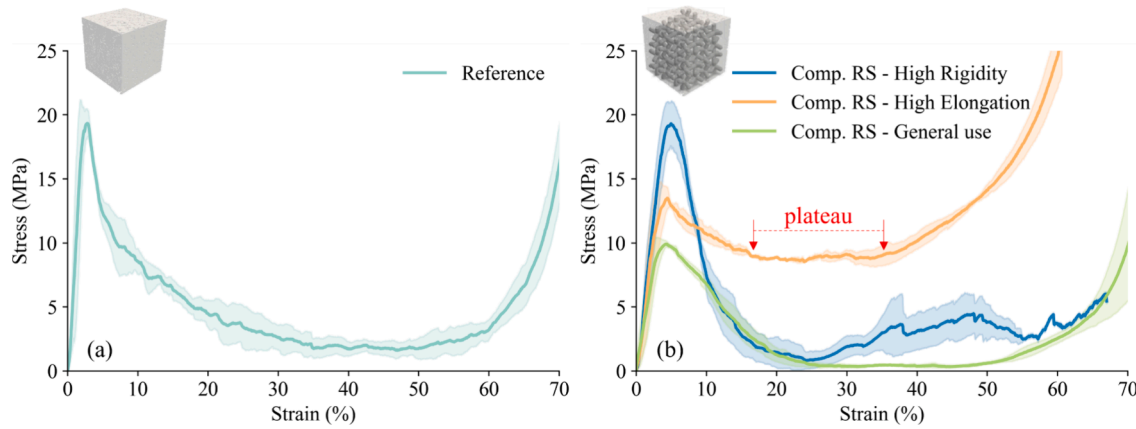
Fig. 13. Stress–strain curves for reference cement mortar (a) and cementitious composites with auxetic reinforcement printed using different resin formulations (b) where the solid line denotes the average values and shaded area indicates the deviation.

deformable materials to manufacture auxetic lattices to enable the proper function in cementitious composites.

Fig. 14 presents the compressive stress–strain curves of cementitious composites reinforced with different architectures of 3D printed lattice structures, using the high elongation resin as the printing material. It can be seen from the figure that, in contrast to the non-auxetic structures (octet and cubic), the stress–strain curves for auxetic lattice reinforced cementitious composites showed a distinct peak before transitioning into the plateau stage, while the composites with non-auxetic lattice reinforcement went directly into the plateau stage. This may be attributed to the confinement effect provided by the negative Poisson's ratio of the auxetic lattice structures. The auxetic lattices tend to contract laterally under compression, which could constrain the expansion of cementitious matrix and lead to an increase in stress. However, with the increase of compressive strain, the constrain gradually reduced due to the relatively lower stiffness of auxetic lattices compared to cement matrix. The detailed explanations will be provided in Section 4. In addition, although higher than non-auxetic lattice reinforced composites, the strength for auxetic lattice reinforced composites was lower compared to the reference cement mortar. However, the area under the stress–strain curves were still higher compared to the reference group. This is beneficial when the intended application scenario is for energy absorption or impact resistance. In these cases, a higher area under the curve can be more important than the peak strength. Admittedly, the
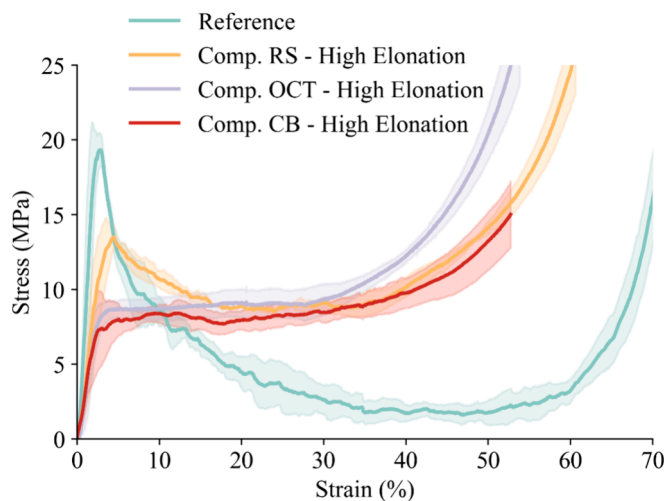
peak strength is somewhat reduced by introducing a softer polymer-based materials into the cementitious matrix, but this trade-off suggests that auxetic cementitious composites could be applied in scenarios where post-peak ductility is more important. More detailed discussion of the energy absorption capacity will be discussed in the following section.

3.3.2. Energy absorption capacity

Fig. 15(a) illustrates a typical compressive stress–strain curve for cementitious composites reinforced with lattices printed using the high elongation resin, which can be divided into three stages: ascending stage, plateau stage, and densification stage. In the densification stage, the cementitious composites become fully compacted, where the stiffnesses drastically increase and stresses increase exponentially, showing that the material would act more rigidly and lose its ability to further effectively absorb energy. As mentioned above, the onset strains of the densification stage are different for composites with different lattice architectures and printing materials. Therefore, to compare the ultimate energy absorption capacity for lattice-reinforced cementitious composites with different materials and architectures, the densification energy defined as the energy absorption before reaching densification stage was used here. In this study, the energy absorption efficiency was utilized to determine the onset strain of densification stage [47,48], which can be expressed as

$$\eta(\varepsilon) = \frac{1}{\sigma(\varepsilon)} \int_0^\varepsilon \sigma(\varepsilon) \mathrm{d}\varepsilon \qquad (1)$$

where η is the energy absorption efficiency as a function of strain ε; σ is the stress as a function of strain. Fig. 15(b) shows the calculated energy absorption efficiency, and the onset strain of densification stage ε_d can be therefore determined as

$$\frac{\mathrm{d}\eta(\varepsilon)}{\mathrm{d}\varepsilon}\bigg|_{\varepsilon=\varepsilon_d} = 0 \qquad (2)$$

which indicates that the onset strain corresponds to the strain level where the energy absorption efficiency η reaches its local maximum. In other words, when the strain exceeds the onset strain, the energy absorption efficiency begins to decline due to the exponential increase in stress, indicating the beginning of the densification stage. The densification energy E is defined integration of stress–strain curves until the onset strain of densification, multiplied by the sample volume (V).

$$E = V \bullet \int_0^{\varepsilon_d} \sigma(\varepsilon) \mathrm{d}\varepsilon \qquad (3)$$

The densification energies for cementitious composites reinforced with

Fig. 14. Stress–strain curves for reference cement mortar and cementitious composites with auxetic lattices (rotating square, RS) and non-auxetic lattices (octet, OCT; and cubic, CB).
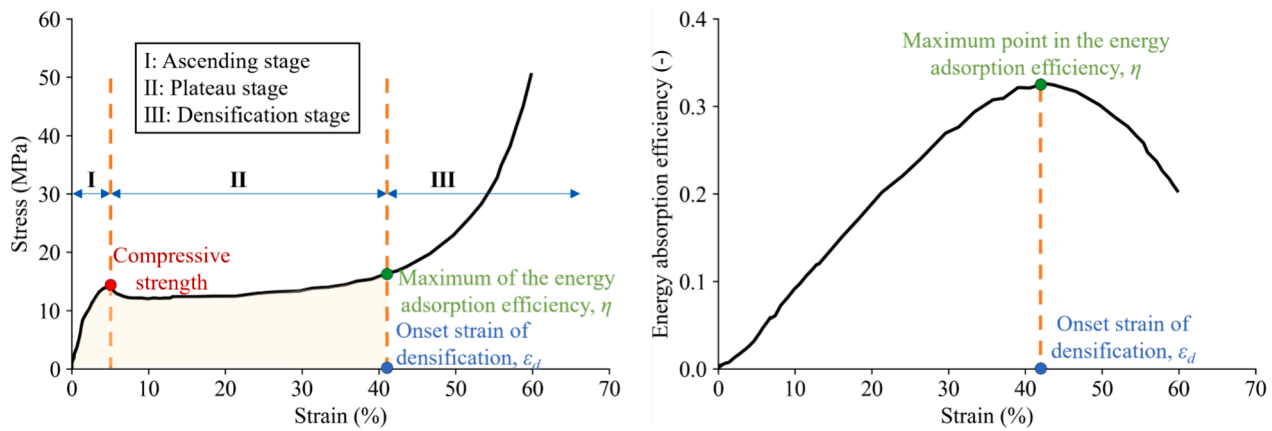
Fig. 15. Representative stress–strain curves for cementitious composites with lattices printed by resin with high elongation capacity (a), and energy absorption efficiency to determine the onset strain of densification stage (b).

auxetic lattices printed by different resins are shown in Fig. 16(a). Compared to the reference sample without reinforcement, the densification energy for samples with auxetic lattices with high elongation capacity was 1.68 times that of reference mortar. However, when general-purpose resin or high rigidity resin was used, the densification energy was lower. This reduction is attributed to the embedded lattices breaking during the loading process, which introduced defects within the matrix, resulting in a relatively lower plateau stress. Additionally, Fig. 16(b) shows the effect of different lattice architectures printed with the high elongation resin on densification energy. The rotating square architecture demonstrated the most significant improvement in densification energy for cementitious composites. Although the octet and cubic structures also enhanced densification energy compared to the reference, their average values were lower than those with rotating square. This could be caused by the stress peak observed in cementitious composites with auxetic lattices, while composites with non-auxetic structures transitioned directly to the plateau stage as shown in Fig. 14.

3.3.3. Correlation analysis

To better understand the interplay between the properties of lattice structures and those of cementitious composites, the average values of densification energy and strength (peak stress) were compared via heat maps in Fig. 17. The stress–strain curves for the corresponding cementitious composite samples are provided in Appendix B. It can be clearly seen that, when using the resin with high elongation capacity, the auxetic lattice structures exhibited superior performance in improving both densification energy and strength compared to the other two non-auxetic structures. However, in cases where a high rigidity resin or a

general-purpose resin were employed, the benefits of the auxetic rotating square lattice become less apparent and can sometimes lead to poorer performance compared to non-auxetic structures. This is related to the mechanisms underlying the auxetic behavior in 3D-printed lattice structures. Achieving auxetic behavior often requires significant local deformation, such as buckling at the strut joints in this study. However, brittle materials can cause abrupt fractures at these joints, turning the broken struts into flaws within the cementitious matrix and ultimately reducing the load-bearing capacity of the composites.

For non-auxetic lattices such as cubic shaped ones, when the resin of high rigidity was used, the strength could reach 29.92 MPa which is far higher than that of the cementitious matrix (around 20 MPa). This enhancement can be attributed to the inclination of cubic-shaped lattice architecture with the loading direction, which reduces the likelihood of buckling under compression. In this scenario, the benefits of high rigidity and strength from the printing materials can be fully harnessed, as they are not diminished by the buckling tendency observed in auxetic lattices. This mechanism is further supported by the results observed with the other two materials (i.e., the high-elongation and general-purpose resins). In these cases, cubic-shaped lattices did not contribute to strength improvement. This is primarily because the lower strength and stiffness of these resins make the lattices more susceptible to tilting under compression, either through buckling or cracking as shown in Fig. 9(f) and Fig. 9(i), so their contribution after embedded inside the cement matrix is also less significant. Overall, these results underscore the importance of both base material properties and lattice structure design in determining the mechanical performance of cementitious composites, which indicates the potential to design
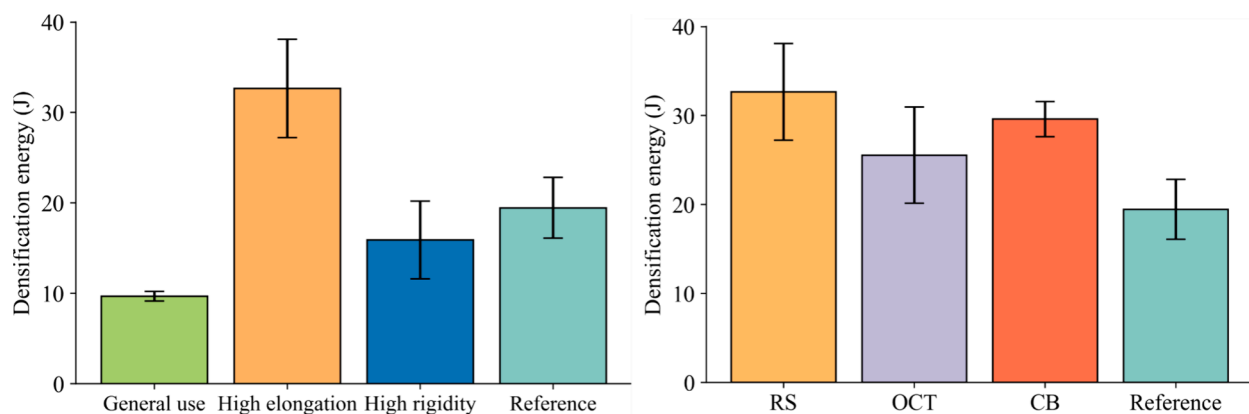

Fig. 16. Densification energy: (a) cementitious composites with auxetic lattices printed by different resins, and (b) cementitious composites with different architectures printed by the high elongation resin.
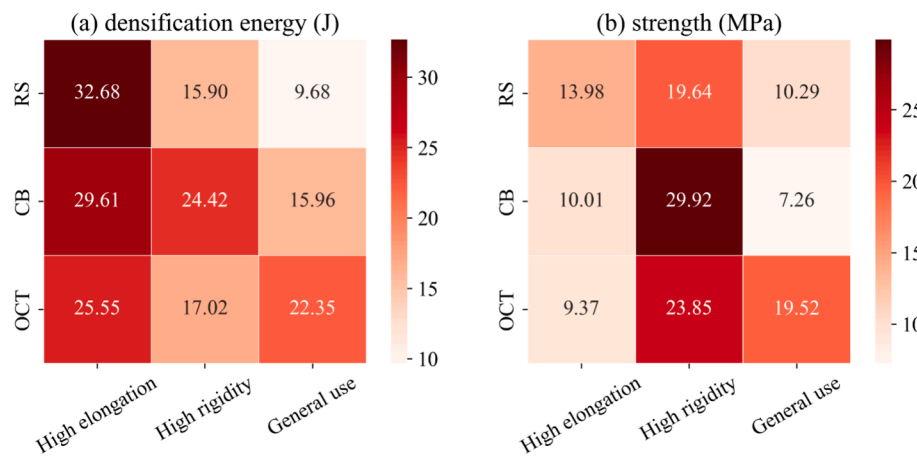
Fig. 17. Heat maps for cementitious composites with 3D printed lattice structures: (a) densification energy and (b) strength.

cementitious composites with a diverse range of properties by considering the properties of the base material and the architecture of embedded lattice structures.

4. CT scanning analysis

To further unravel the underlying mechanisms of the mechanical properties for cementitious composites embedded with auxetic lattice structures, the ex-situ CT test was utilized to monitor the internal damage conditions. Two cementitious samples embedded with rotating square (auxetic) and octet (non-auxetic) lattices printed by resin with high elongation capacity were prepared. Each sample was loaded to the strain levels of 2.5 %, 5 %, and 7.5 % respectively, and after reaching every strain level, the two specimens were then unloaded and taken for the CT scanning, which constitutes a total of six CT scans.

4.1. Crack distributions

The cracks within cementitious composites featuring auxetic and non-auxetic lattice structures under different strain levels are visualized in Fig. 18. The vertical view where the 3D printed lattice structures have

been hided is displayed for a clear observation of cracks. The color bars in the figure show the crack volume distributions segmented by the 6-connected connectivity criterion (face-based connectivity). Essentially, a voxel is considered connected to another voxel if they share a face, so the single crack identified in this study is made up of multiple voxels that are connected along one face to the neighboring voxels. The detailed explanations on the 6-connected connectivity can be found in Appendix C.

When the samples were compressed to a strain of 2.5 %, cracks were already evident within the matrix. In cementitious composites reinforced with rotating square lattices, the cracks are more likely to be distributed on the outer side of the specimen, and only a few minor cracks were observed in the core area. This is beneficial since, if the core remains less damaged, it can continue to bear loads and distribute stresses, and ensure the composites remain functional for resisting subsequent events. However, in composites with non-auxetic octet lattices, the crack distribution was more extensive. This suggests that the auxetic behavior of the rotating square lattice structures can confine the lateral expansion of cementitious matrix under uniaxial compression, leading to less damage in the cement matrix. The non-auxetic octet structure will expand together with the matrix and thus lacks the
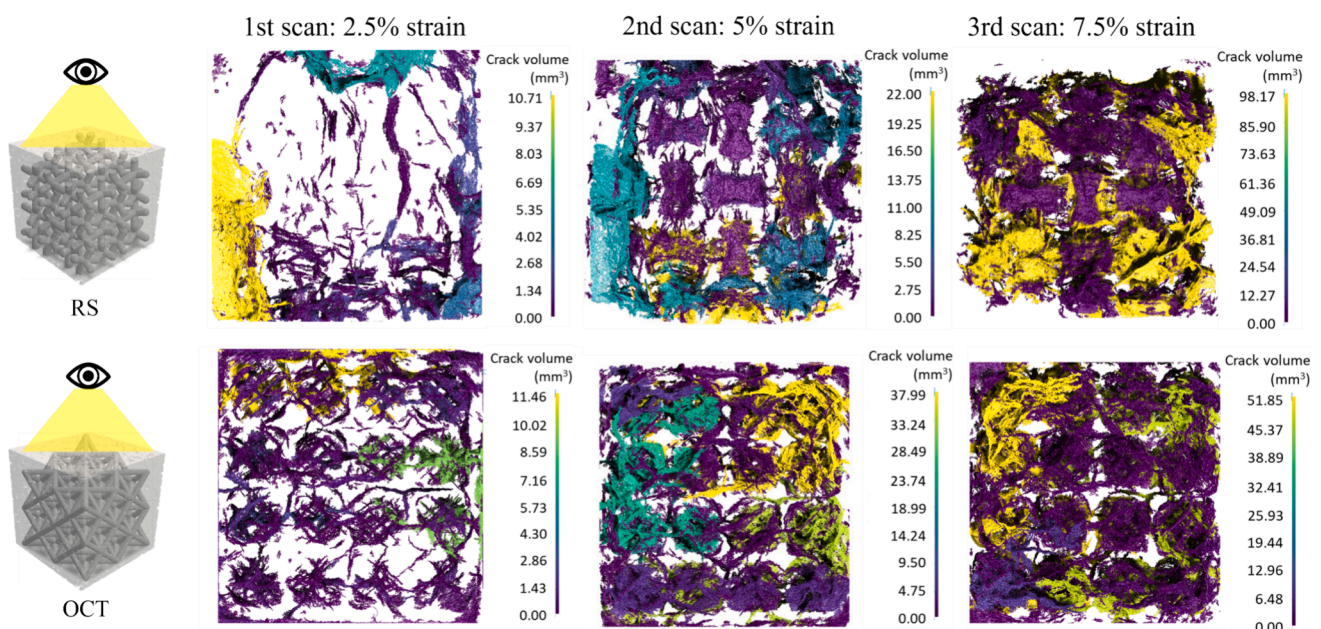

Fig. 18. Cracks inside the cementitious composites with auxetic (top row) and non-auxetic (bottom row) lattice structures.

confining capability of the auxetic structure. This less damaged matrix induced by auxetic lattices could also explain the fact that there is an obvious stress peak for cementitious composites reinforced with rotating square structures, as observed from Fig. 14, while others transitioned directly to the plateau stage. Upon reloading the sample to a strain of 5 %, cracks started to emerge in the core area of composites reinforced with auxetic lattices. However, most of the cracks in the core area were tiny cracks, and some larger cracks have formed at the outside area, as indicated by the color bar. This indicates that, with the increase of compressive strain, the confinement from auxetic lattice structure gradually reduces. Due to the lack of confinement at the outside area (such as the corners and the surface which were not fully reinforced by the lattices), the cracks started to propagate. For composites with octet lattice, cracks progressively interconnected to form larger cracks penetrating the core area. Upon reloading to a strain of 7.5 %, large cracks were observed in the core area in both cases.

4.2. Crack volumes

Crack volume distributions under the compressive strain of 2.5 %, 5.0 % and 7.5 % are displayed in Fig. 19. It should be noted that, to compare the confining effect of auxetic lattice structures, the region of interest (ROI) here was selected as a cube shaped 17 mm × 17 mm × 17 mm, as shown in Fig. 19(d). This is because the exterior layer was not completely reinforced by the 3D printed lattices, and thereby cracks first, but the interior core was effectively confined by the surrounding lattice structures and is more representative to compare the confinement effect. It can be seen from Fig. 19(a) that, when the compressive strain reached 2.5 %, the cracks in auxetic lattice reinforced cementitious composites were distributed within a smaller volume range, in which the maximum crack volume was around 3 mm³. On the contrary, the cracks in cementitious composites with non-auxetic octet structure reached more than 10 mm³. Therefore, it can be indicated that it is the auxetic

behavior from the RS lattice that can lead to a less damaged cementitious matrix. When the specimens were reloaded to 5.0 % strain, larger cracks started to form in composites with auxetic lattice, where one crack with a volume of 16 mm³ has appeared. Nevertheless, the crack volume distribution trend for auxetic lattice reinforced composites is still more leftwards shifted. In other words, the median number for crack volume of composites with auxetic lattices (0.12 mm³) was smaller than that of composites reinforced with positive Poisson's ratio lattices (0.23 mm³), suggesting that the auxetic lattices can still limit crack development in the cementitious matrix. However, when the strain was increased to 7.5 %, no difference can be found in the crack volume distributions, which indicates that the confinement from the negative Poisson's ratio lattice was not that effective at such a strain level.

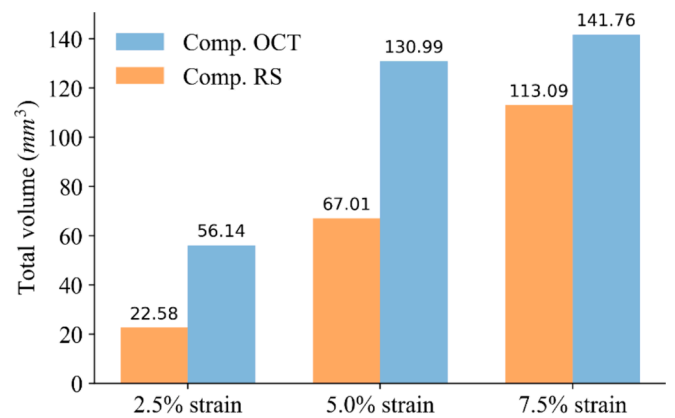In addition, the total crack volumes have also been compared in

Fig. 20. Crack volumes for cementitious composites with non-auxetic octet and auxetic rotating square lattice structures.
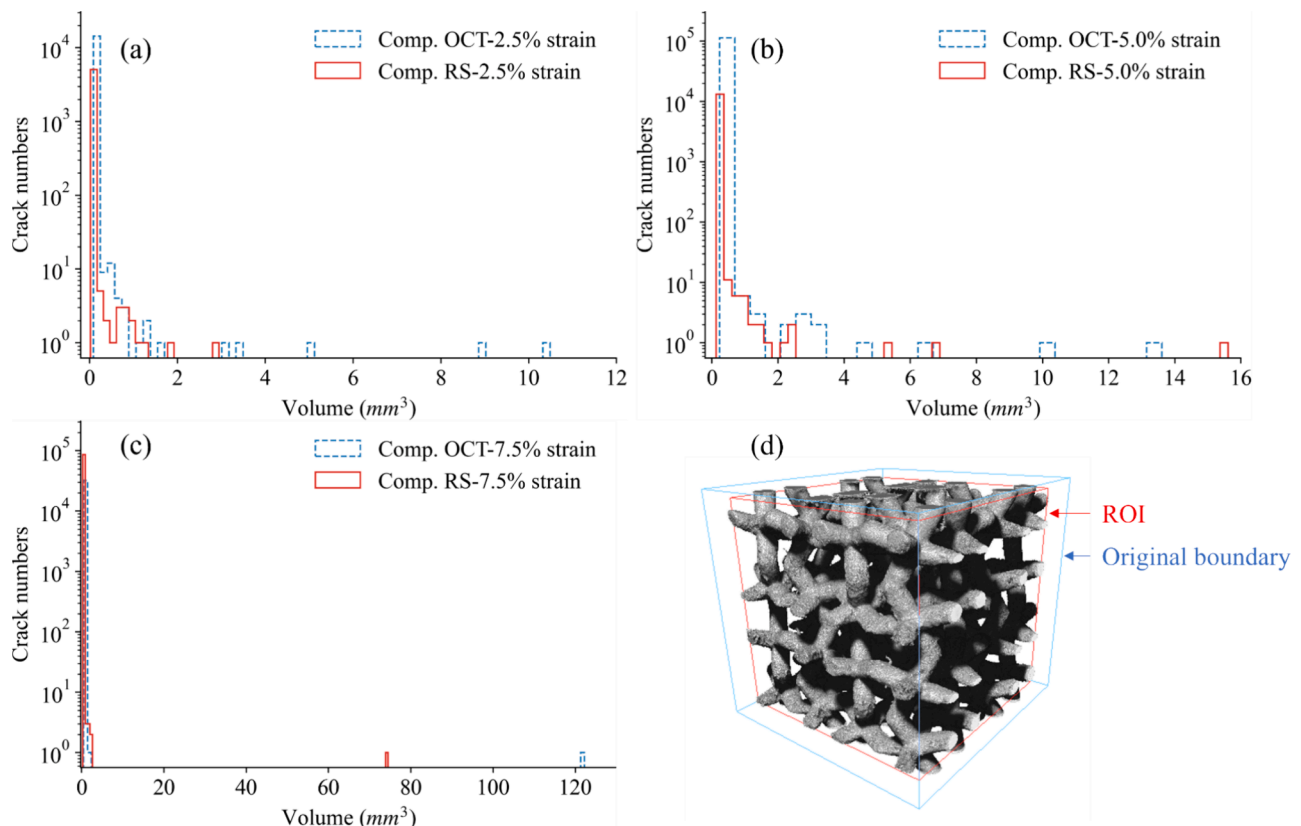
Fig. 19. Crack volume distributions at compressive strains of (a) 2.5%, (b) 5.0%, (c) 7.5%, and (d) selection of the region of interest.

Fig. 20. At a strain of 2.5 %, composites with octet lattices showed a higher total crack volume compared to composites with auxetic rotating square lattices. This indicates that auxetic lattice structures can reduce damage degree and maintain structural integrity better than the non-auxetic structures. With the increase of strains, although the gap between compositions with different lattices narrowed slightly, cementitious composites reinforced with rotating square lattice still demonstrated a smaller crack volume, which indicates its potential application where high resistance to cracking under severe strain conditions is required.

4.3. Microstructural damage mechanisms

To further discuss the microstructural damage mechanisms in composites reinforced by different lattice structures, crack distributions are displayed by slicing on three parallel planes at an interval of 5 mm along the ZY direction and XY direction. The CT scanning results at a strain level of 2.5 % have been selected, and the corresponding states at the stress–strain curve are illustrated in Fig. 21. At this strain level, the non-auxetic lattice-reinforced composites begin transitioning into the plateau stage, whereas the auxetic lattice-reinforced composites remain in the ascending phase, approaching their peak strength.

Fig. 22 shows the microstructural damage of auxetic lattice reinforced cementitious composites. In the ZY planes, particularly those closer to the out surface of the specimens (left and right planes), cracks were more dispersed. This dispersion is primarily attributed to the lack of confinement provided by the lattice structure in the exterior regions of the composite. In contrast, the central ZY plane shows vertical cracks initiated from the joints. As highlighted by the arrows in Fig. 22(b), these vertical cracks are primarily caused by indentation from the lattice joints. The indentation creates localized tensile forces within the cement matrix, resulting in cracks that resemble tensile splitting cracks. However, these vertical cracks did not penetrate through the entire specimen, but were limited within the unicell of the auxetic lattice. This is because the adjacent lattice joints eventually come into contact, forming a new confinement that stabilizes the cement matrix on both sides of the crack.

The XY plane provides additional insights into the influence of the auxetic lattice on microstructural damage. Similar with the observations at left and right planes on ZY direction, cracks appear to be more concentrated at the exterior region of the composites. As the auxetic structure contracts inward under load, the cement matrix tends to expand outward due to its natural deformation behavior (i.e., positive Poisson's ratio). This opposing deformation between the lattice and the matrix leads to the peeling of the matrix's exterior layer. However, in the interior, the lattice and matr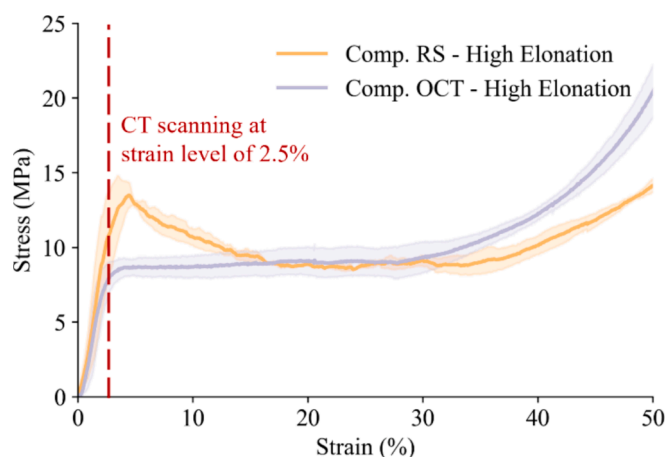ix mutually constrain this inverse deformation, resulting in fewer cracks distributed in the core area. This interaction between the inward-contracting lattice and the outward-expanding matrix creates a stabilizing effect that reduces crack development and contributes to the improved mechanical performance of the auxetic lattice-reinforced composite.

The microstructural damage observed in non-auxetic octet lattice reinforced cementitious composites is illustrated in Fig. 23. Compared to composites reinforced with auxetic lattices, these non-auxetic lattice-reinforced composites exhibit a greater number of vertical cracks, especially in the ZY planes. The formation and distribution of these vertical cracks are closely linked to the deformation behavior of the lattice structure under compression. As indicated by the blue dashed line, which outlines the deformed shape of the unit cell, the outward displacement of the lattice nodes during compression leads to localized compression of the cement matrix near the nodes. However, the surrounding reinforcement fails to provide adequate confinement due to its outward-expanding tendency, a characteristic of the non-auxetic structure. This lack of confinement exacerbates the development of vertical cracks along the ZY planes.

In the XY planes, the damage is predominantly characterized by interfacial damage between the octet lattice reinforcement and the cement matrix. This type of damage is in contrast with the crack patterns observed in auxetic lattice-reinforced composites. The underlying reason for this difference lies in the higher positive Poisson's ratio of the non-auxetic octet structure (above 0.3), which indicates a greater lateral expansion tendency compared to the cement matrix. This larger lateral deformation tendency of the octet lattice also explains the more significant interfacial debonding and subsequent interfacial crack propagation. As a result, the lattice reinforcement fails to provide lateral confinement to the matrix, which increases the likelihood of shear crack formation under uniaxial compression.

In comparison, the non-auxetic octet reinforced cementitious composites showed more severe vertical cracks, and more significant interfacial damage were observed at both interior and exterior areas of the composites. This indicates the auxetic lattice showed a better composite action with the cement matrix, and it also explains the reason that the auxetic lattice reinforced composites showed a higher stress than the non-auxetic counterpart at a strain of 2.5 %. In addition, the energy dissipation characteristics of the lattice reinforced composites are also influenced by these microstructural damage mechanisms. Due to a larger number of vertical cracks and the significant interfacial damage, the non-auxetic lattice reinforced composites tend to dissipate energy through the extensive propagation of cracks and the interfacial frictions between the lattice structure and the cement matrix. In contrast, due to the inward-contracting behavior, auxetic lattice reinforced cementitious composites tend to dissipate energy more efficiently by constraining crack growth and distributing stress more evenly in the cement matrix, which allows the material to dissipate energy over a larger volume.

5. Conclusions

This study explores auxetic lattices that can be used as reinforcement in cementitious composites to provide higher load bearing capacity and damage dissipation than the non-auxetic counterparts. The uniaxial compression tests were conducted on cementitious composites reinforced with 3D printed auxetic and non-auxetic lattices. The multidirectional auxetic lattice was designed to have a negative Poisson's ratio in all directions, and non-auxetic lattices with a similar volume were also included for comparison. In addition, to investigate the influence of mechanical properties of the lattice structures, the lattices were printed with base materials featuring distinctly different stiffnesses and deformation capacities. To better understand the reinforcing mechanisms of the auxetic lattice structures in cementitious matrix, micro CT scanning was carried out under three different compressive strains, and the crack distribution patterns and volumes were analyzed to gain a deeper understanding of the micro-cracking and failure mechanisms for
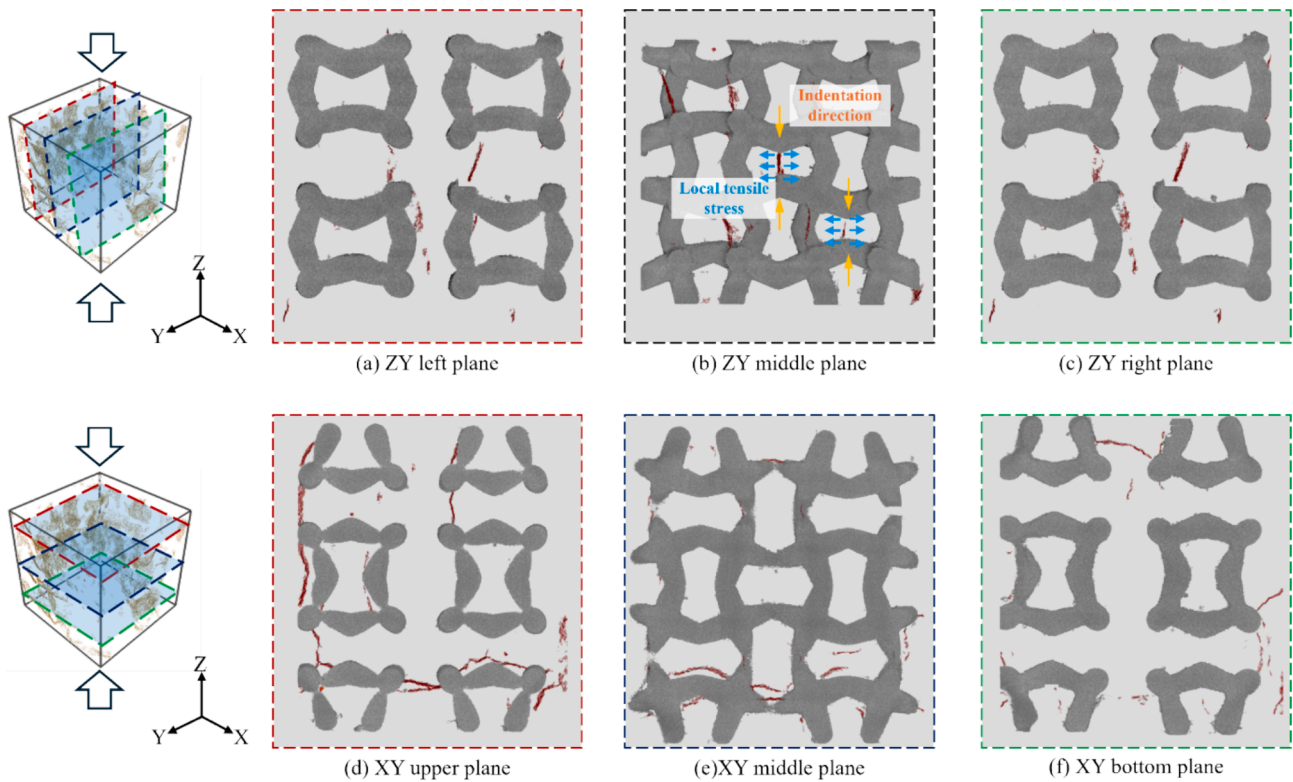

Fig. 21. Stress state at a strain level of 2.5% where the CT scanning was selected for microstructural analysis.

Fig. 22. Microstructural damage situations for cementitious composites with auxetic rotating square lattice on different slice planes, where gray components represent the lattice and red components represent the cracks. (For interpretation of the references to color in this figure legend, the reader is referred to the web version of this article.)
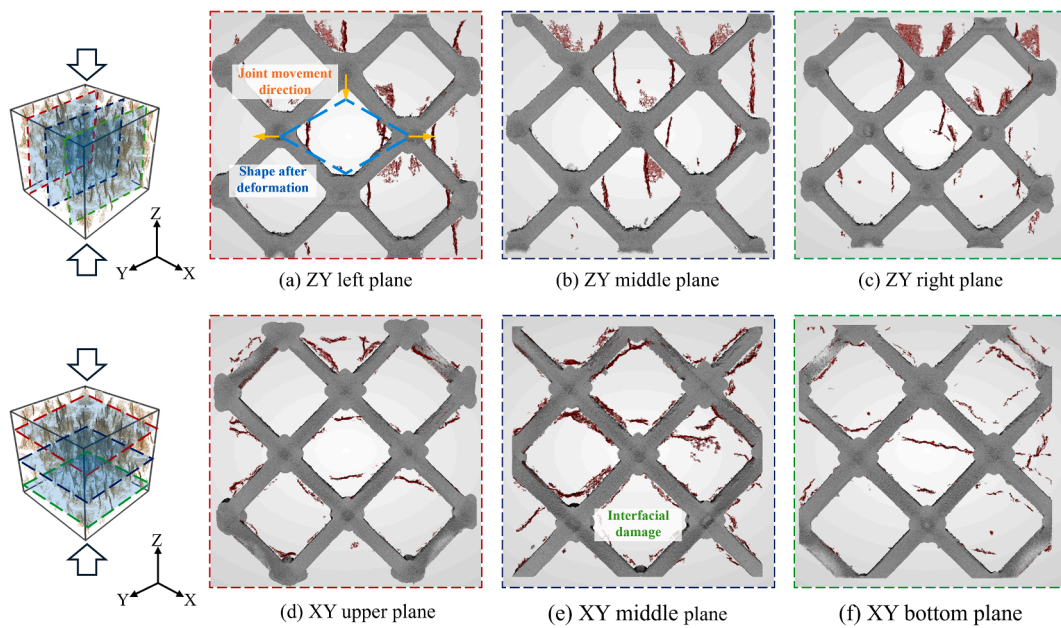

Fig. 23. Microstructural damage situations for cementitious composites with non-auxetic octet lattice on different slice planes, where gray components represent the lattice and red components represent the cracks. (For interpretation of the references to color in this figure legend, the reader is referred to the web version of this article.)

cementitious composites with auxetic lattices. The conclusions can be summarized as follows.

1) According to the micro CT characterization, the ductile cracking mechanism was found to explain the peak stress and improved post-

peak ductility for cementitious composites reinforced by auxetic lattices. At a strain level of 2.5 %, the cracks were more disconnectedly distributed, and the crack volume insides the core of auxetic lattice reinforced composites was 60 % lower than these with non-auxetic lattices. With the increase of strain level up to 5 %, the

auxetic lattice can still mitigate crack merging and local failure of cement matrix. When the strain reached 7.5 %, although the effect on limiting crack as disconnected was no longer obvious, the lattice structure could still contribute to maintain the integrity of composite materials, with the total crack volume was still 20 % lower compared to cementitious composites with non-auxetic lattice structures.

2) The damage dissipation energy mechanisms were found to be different in auxetic and non-auxetic lattice reinforced cementitious composites. Because of lack of lateral confinement on cement matrix, the non-auxetic octet lattice reinforced cementitious composites tend to dissipate energy through extensive propagation of cracks and interfacial damages between the lattice and the cement matrix. In contrast, due to the inward-contracting behavior, auxetic rotating square lattice reinforcement showed a better composite action with the matrix, so the composites tend to dissipate energy by constraining crack growth and distributing stress more evenly in cement matrix.

3) The auxetic lattice structures can compensate the strength reduction caused by introducing a relatively soft and deformable material into the cementitious matrix. Conversely, when a stiff and brittle printing base material was adopted, the performance of the auxetic lattices in enhancing the composite material's strength dimished. This decline was primarily attributed to fractures at the joints of auxetic lattice structures, which precipitated the structural failure of the composites.

4) When using a printing material with high deformability, the auxetic lattice reinforced cementitious composites showed superior post-peak ductility and densification energy absorption capacity compared to the plain cement mortar, and composites reinforced with non-auxetic lattice structures. However, when the printing material did not have enough deformability to enable the auxetic behavior of lattice structures, the improvement in energy absorption capacity of the composites was not significant not even if the lattices were designed to be auxetic.

This study designs the enhanced energy absorbing cementitious composites by embedding auxetic lattice structures. Compared to traditional methods such as fiber or steel reinforcements, 3D printing offers greater precision and customization, ensuring high-quality auxetic lattices that can be tailored to fit specific forms, reducing the need for on-site adjustments. However, steel and fibers are widely available, often leading to lower material costs due to economies of scale. Steel and fiber reinforcement methods are more scalable, while the 3D printed lattices are currently limited on smaller scales, making them only applicable to small areas and less cost-effective in larger projects. Future improvements could involve in-situ CT tests to avoid crack closure caused by unloading, offering more detailed insights into internal composite action. Additionally, exploring alternative printing methods to manufacture larger auxetic lattices and investigating their suitability for application in larger scales is also recommended, along with further research into the size effect and other influencing factors on lattice performance.

CRediT authorship contribution statement

Zhaozheng Meng: Writing – review & editing, Writing – original draft, Visualization, Software, Methodology, Investigation, Formal analysis, Data curation, Conceptualization. **Yading Xu:** Writing – review & editing, Visualization, Methodology, Investigation, Formal analysis. **Jinbao Xie:** Writing – review & editing, Software, Methodology, Investigation, Formal analysis. **Wen Zhou:** Writing – review & editing, Investigation, Formal analysis, Conceptualization. **Rowin J.M. Bol:** Writing – review & editing, Methodology, Investigation, Conceptualization. **Qing-feng Liu:** Writing – review & editing, Visualization, Methodology. **Branko Šavija:** Writing – review & editing, Supervision, Resources, Project administration, Methodology, Investigation, Funding acquisition, Formal analysis, Conceptualization.

Declaration of competing interest

The authors declare that they have no known competing financial interests or personal relationships that could have appeared to influence the work reported in this paper.

Data availability

Data will be made available on request.

Acknowledgements

Appendix A

The printing layer view of the dog bone specimens by material extrusion method is shown in Fig. A1. More detailed information about the printing parameters can be found in reference [35].

Fig. A1. Printing layer view of dog bone specimen printed by MEX method.

Appendix B

The stress–strain curves for cementitious composites reinforced with lattices printed by different materials are shown in the figures below. Fig. B1 shows the stress–strain curves for cementitious composites reinforced by cubic lattices, and Fig. B2 shows the stress–strain curves for cementitious composites reinforced by octet lattices, and Fig. B3 shows the stress–strain curves for cementitious composites reinforced by rotating square lattices. In

these figures, blue lines denote the high rigidity resin, green lines denotes the general-purpose resin, and orange lines denote the high elongation resin.
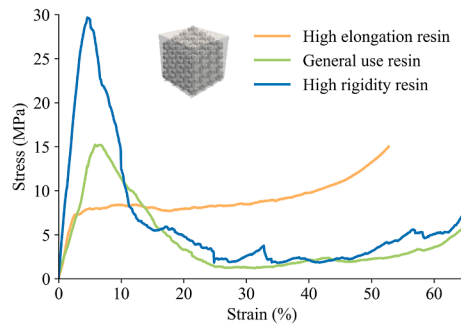

Fig. B1. Stress–strain curves for cementitious composites with cubic lattices printed by different materials.
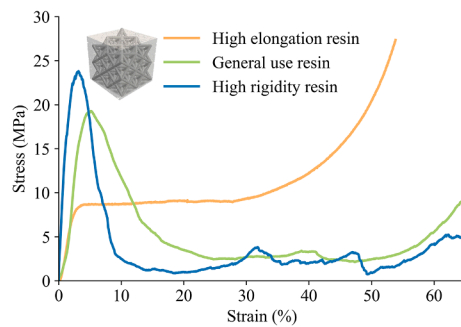

Fig. B2. Stress–strain curves for cementitious composites with octet lattices printed by different materials.
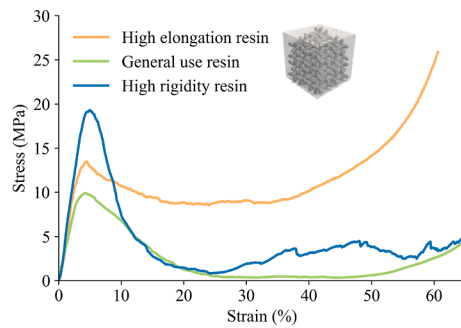

Fig. B3. Stress–strain curves for cementitious composites with rotating square lattices printed by different materials.

Appendix C

The basic principles of the 6-connected criterion is shown in the figure below. For two voxels which can be considered as 6-connected, these two voxels must share a face, indicating that that they are directly touching each other along one of their six faces. Conversely, if two voxels only share edges or corners, they are labelled as separate parts. The choice of connectivity criterion would affect the results of connectivity-based analysis, but the 6-connection criterion is less computationally intensive and ensures that connected components are more clearly defined.
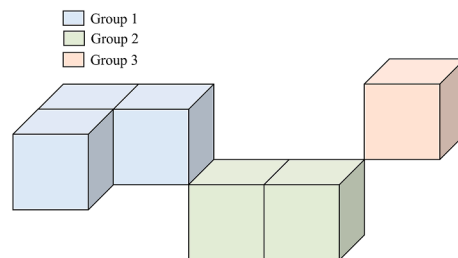

Fig. C1. Illustrative diagram of the 6-connection criterion.

References

[1] Y. Yuan, S. Ma, X. Sun, B. Chen, Y. Luo, Z. Lin, Y. Liang, 3D printed auxetic metamaterials with tunable mechanical properties and morphological fitting abilities, Mater. Des. 244 (2024) 113119.

[2] J.B. Xie, Y.D. Xu, Z. Wan, A. Ghaderiaram, E. Schlangen, B. Savija, Auxetic cementitious cellular composite (ACCC) PVDF-based energy harvester, Energ. Buildings 298 (2023).

[3] M. Moini, J. Olek, J.P. Youngblood, B. Magee, P.D. Zavattieri, Additive Manufacturing and Performance of Architectured Cement-Based Materials, Adv. Mater. 30 (43) (2018).

[4] Z.P. Bazant, J. Planas, Fracture and Size Effect In Concrete And Other Quasibrittle Materials, Routledge, 2019.

[5] Q. Fu, Z.H. Wang, Z.M. Zhou, D.T. Niu, Y. Wang, Feasible brittleness evaluation method and suggestion for brittleness reduction of cementitious materials based on stress-strain curve, Arch. Civ. Mech. Eng. 22 (4) (2022).

[6] M. Lukovic, E. Schlangen, G. Ye, Combined experimental and numerical study of fracture behaviour of cement paste at the microlevel, Cement Concr. Res. 73 (2015) 123–135.

[7] D.R. Ren, X.L. Liu, B.Q. Cui, E.Z. Wang, Q. Ma, F.Y. Yan, W.Q. Xie, Meso-crack evolution based constitutive model for concrete material under compression, Compos. Part B-Eng. 265 (2023).

[8] Y.Y.Y. Cao, G. Liu, H.J.H. Brouwers, Q.L. Yu, Enhancing the low-velocity impact resistance of ultra-high performance concrete by an optimized layered-structure concept, Compos. Part B-Eng. 200 (2020).

[9] F. Bester, M. van den Heever, J. Kruger, G. van Zijl, Reinforcing digitally fabricated concrete: A systems approach review, Addit. Manuf. 37 (2021).

[10] Y.W. Liu, Z.H. Zhang, C.J. Shi, D.J. Zhu, N. Li, Y.L. Deng, Development of ultra-high performance geopolymer concrete (UHPGC): Influence of steel fiber on mechanical properties, Cement Concr. Comp. 112 (2020).

[11] L.G. Li, B.F. Xiao, Z.Q. Fang, Z. Xiong, S.H. Chu, A.K.H. Kwan, Feasibility of glass/basalt fiber reinforced seawater coral sand mortar for 3D printing, Addit. Manuf. 37 (2021).

[12] Z.Z. Meng, Q.F. Liu, J. Xia, Y.X. Cai, X.J. Zhu, Y. Zhou, L. Pel, Mechanical-transport-chemical modeling of electrochemical repair methods for corrosion-induced cracking in marine concrete, Comput-Aided Civ. Inf. 37 (14) (2022) 1854–1874.

[13] B. Zhou, Y. Uchida, Relationship between fiber orientation/distribution and post-cracking behaviour in ultra-high-performance fiber-reinforced concrete (UHPFRC), Cement Concr. Comp. 83 (2017) 66–75.

[14] C. Tang, J. Liu, W. Hao, Y. Wei, Flexural properties of 3D printed graded lattice reinforced cementitious composites using digital image correlation, Mater. Des. 227 (2023).

[15] B. Salazar, P. Aghdasi, I.D. Williams, C.P. Ostertag, H.K. Taylor, Polymer lattice-reinforcement for enhancing ductility of concrete, Mater. Des. 196 (2020).

[16] A. Jipa, L. Reiter, R.J. Flatt, B. Dillenburger, Environmental stress cracking of 3D-printed polymers exposed to concrete, Addit. Manuf. 58 (2022).

[17] D. Dey, V.N. Van, H.N. Xuan, D. Srinivas, B. Panda, P. Tran, Flexural performance of 3D printed concrete structure with lattice infills, Dev. Built Environ. 16 (2023).

[18] Y.D. Xu, H.Z. Zhang, Y.D. Gan, B. Savija, Cementitious composites reinforced with 3D printed functionally graded polymeric lattice structures: Experiments and modelling, Addit. Manuf. 39 (2021).

[19] S.Q. Ma, S. Fu, Q.K. Wang, L. Xu, P.G. He, C.Y. Sun, X.M. Duan, Z.H. Zhang, D. C. Jia, Y. Zhou, 3D printing of damage-tolerant martian regolith simulant-based geopolymer composites, Addit. Manuf. 58 (2022).

[20] E.O. Momoh, A. Jayasinghe, M. Hajsadeghi, R. Vinai, K.E. Evans, P. Kripakaran, J. Orr, A state-of-the-art review on the application of auxetic materials in cementitious composites, Thin-Walled Struct. 196 (2024).

[21] K.E. Evans, A. Alderson, Auxetic materials: Functional materials and structures from lateral thinking!, Adv. Mater. 12 (9) (2000) 617–628.

[22] Y. Prawoto, Seeing auxetic materials from the mechanics point of view: A structural review on the negative Poisson's ratio, Comp. Mater. Sci. 58 (2012) 140–153.

[23] G.A. Lyngdoh, N.K. Kelter, S. Doner, N.M.A. Krishnan, S. Das, Elucidating the auxetic behavior of cementitious cellular composites using finite element analysis and interpretable machine learning, Mater. Des. 213 (2022).

[24] M. Chen, S. Fang, G. Wang, Y. Xuan, D. Gao, M. Zhang, Compressive and flexural behaviour of engineered cementitious composites based auxetic structures: An experimental and numerical study, J. Build. Eng. 86 (2024).

[25] X.C. Teng, X. Ren, Y. Zhang, W. Jiang, Y. Pan, X.G. Zhang, X.Y. Zhang, Y.M. Xie, A simple 3D re-entrant auxetic metamaterial with enhanced energy absorption, Int. J. Mech. Sci. 229 (2022).

[26] C. Iantaffi, E. Bele, D. Mcarthur, P.D. Lee, C.L.A. Leung, Auxetic response of additive manufactured cubic chiral lattices at large plastic strains, Mater. Des. 233 (2023).

[27] N. Li, S.Z. Liu, X.N. Wu, J.Y. Wang, Y.S. Han, X.C. Zhang, Mechanical characteristics of a novel rotating star-rhombic auxetic structure with multi-plateau stages, Thin-Walled Struct. 191 (2023).

[28] K.E. Evans, Auxetic polymers: a new range of materials, Endeavour 15 (4) (1991) 170–174.

[29] S.Q. Yuan, F. Shen, J.M. Bai, C.K. Chua, J. Wei, K. Zhou, 3D soft auxetic lattice structures fabricated by selective laser sintering: TPU powder evaluation and process optimization, Mater. Des. 120 (2017) 317–327.

[30] M. Asad, N. Win, T. Zahra, D.P. Thambiratnam, T.H.T. Chan, Y. Zhuge, Enhanced energy absorption of auxetic cementitious composites with polyurethane foam layers for building protection application, J. Build. Eng. 78 (2023).

[31] T. Zahra, M. Dhanasekar, Characterisation of cementitious polymer mortar - Auxetic foam composites, Constr. Build. Mater. 147 (2017) 143–159.

[32] R. Zhong, X. Ren, X. Yu Zhang, C. Luo, Y. Zhang, Y. Min Xie, Mechanical properties of concrete composites with auxetic single and layered honeycomb structures, Constr. Build. Mater. 322 (2022).

[33] H. Zhou, K. Jia, X. Wang, M.-X. Xiong, Y. Wang, Experimental and numerical investigation of low velocity impact response of foam concrete filled auxetic honeycombs, Thin-Walled Struct. 154 (2020).

[34] G. Zhao, Y. Fan, C. Tang, Y. Wei, W. Hao, Preparation and compressive properties of cementitious composites reinforced by 3D printed cellular structures with a negative Poisson's ratio, Dev. Built Environ. 17 (2024).

[35] Y. Xu, B. Šavija, Auxetic cementitious composites (ACCs) with excellent compressive ductility: Experiments and modeling, Mater. Des. 237 (2024).

[36] Y. Xu, Z. Meng, R.J.M. Bol, B. Šavija, Spring-like behavior of cementitious composite enabled by auxetic hyperelastic frame, Int. J. Mech. Sci. 275 (2024).

[37] T. Li, F. Liu, L. Wang, Enhancing indentation and impact resistance in auxetic composite materials, Compos. B Eng. 198 (2020).

[38] T. Mukhopadhyay, D. Kundu, Mixed-mode multidirectional poisson's ratio modulation in auxetic 3D lattice metamaterials, Adv. Eng. Mater. 24 (5) (2022).

[39] J.P. Lang, D. Han, X.G. Zhang, W. Jiang, Y. Zhang, X.H. Ni, J. Hao, X.C. Teng, X. Ren, A star-shaped tubular structure with multiple-directional auxetic effect, Thin-Walled Struct. 193 (2023).

[40] N. Feng, Y.H. Tie, S.B. Wang, J.X. Guo, A novel 3D bidirectional auxetic metamaterial with lantern-shape: Elasticity aspects and potential for load-bearing structure, Compos. Struct. 321 (2023).

[41] Y. Gao, X.Y. Wei, X.K. Han, Z.G. Zhou, J. Xiong, Novel 3D auxetic lattice structures developed based on the rotating rigid mechanism, Int. J. Solids Struct. 233 (2021).

[42] M. Chen, Z. Chen, Y. Xuan, T. Zhang, M. Zhang, Static and dynamic compressive behaviour of 3D printed auxetic lattice reinforced ultra-high performance concrete, Cement Concr. Compos. 139 (2023).

[43] W. Hao, J. Liu, H. Kanwal, Compressive properties of cementitious composites reinforced by 3D printed PA 6 lattice, Polym. Test. 117 (2023).

[44] X.M. Huang, S.Q. Peng, L.H. Zheng, D.X. Zhuo, L.X. Wu, Z.X. Weng, 3D printing of high viscosity UV-curable resin for highly stretchable and resilient elastomer, Adv. Mater. 35 (49) (2023).

[45] R.J.M. Bol, B. Savija, Micromechanical models for FDM 3D-printed polymers: a review, Polymers 15 (23) (2023).

[46] M. Moini, J. Olek, B. Magee, P. Zavattieri, J. Youngblood, Additive manufacturing and characterization of architectured cement-based Materials via X-ray micro-computed tomography, Rilem Bookser 19 (2019) 176–189.

[47] O. Rahman, B. Koohbor, Optimization of energy absorption performance of polymer honeycombs by density gradation, Compos. Part C-Open 3 (2020).

[48] M. Avalle, G. Belingardi, R. Montanini, Characterization of polymeric structural foams under compressive impact loading by means of energy-absorption diagram, Int. J. Impact Eng 25 (5) (2001) 455–472.